World Academy of Science, Engineering and Technology
International Journal of Civil and Environmental Engineering
Vol:10, No:11, 2016

A Failure Criterion for Unsupported Boreholes in Poorly Cemented Granular Formations

Sam S. Hashemi

***Abstract*—**The breakage of bonding between sand particles and their dislodgment from the borehole wall are among the main factors resulting in a borehole failure in poorly cemented granular formations. The grain debonding usually precedes the borehole failure and it can be considered as a sign that the onset of the borehole collapse is imminent. Detecting the bonding breakage point and introducing an appropriate failure criterion will play an important role in borehole stability analysis. To study the influence of different factors on the initiation of sand bonding breakage at the borehole wall, a series of laboratory tests was designed and conducted on poorly cemented sand samples. The total absorbed strain energy per volume of material up to the point of the observed particle debonding was computed. The results indicated that the particle bonding breakage point at the borehole wall was reached both before and after the peak strength of the thick-walled hollow cylinder specimens depending on the stress path and cement content. Three different cement contents and two borehole sizes were investigated to study the influence of the bonding strength and scale on the particle dislodgment. Test results showed that the stress path has a significant influence on the onset of the sand bonding breakage. It was shown that for various stress paths, there is a near linear relationship between the absorbed energy and the normal effective mean stress.

***Keywords*—**Borehole stability, experimental studies, total strain energy, poorly cemented sands, particle bonding breakage

I. Introduction

BOREHOLE stability analysis is one the most challenging topics in geomechanics. Shallow depth boreholes with diameters ranging 100 mm-600 mm and at depths of 30 m-400 m are often drilled for exploration purposes or direct geothermal applications. In vertical loop systems for direct-use of geothermal energy, boreholes are usually no deeper than 150 m [1]. When a borehole is drilled through an unconsolidated formation such as poorly cemented sandy formations, it may collapse within a short period of time (i.e. in an hour to a few months) after drilling is completed depending on the magnitude and direction of the underground flow pressure and/or in situ stresses. If the strength of the cementation between the sand particles is not high enough to withstand the extensile stress concentration the latter may cause grain debonding and this may lead to the borehole failure. Depending on the magnitude of the induced tangential stress around the borehole, the particle dislocation process may diminish after the formation of a stable arch. However, in some cases, especially in deeper boreholes and for reverse faulting stress regimes where $\sigma_H > \sigma_h > \sigma_v$, the arching effect cannot stop the process of particle dislocation and the borehole will collapse completely [2]. Reference [3] identified the driving forces (e.g. in situ stresses and underground fluid flow), formation resisting forces (e.g. friction, cementation and arching effect) and operational approach (e.g. air core drilling and sonic drilling methods) as the main factors affecting the particle debonding at the borehole wall which causes instabilities. [4] numerically simulated the borehole failure in granular materials and showed that the main reason for borehole failure in such formations is the dislocation of particles.

In order to avoid borehole instability, different support systems are employed such as mud pressure, casings and polymers. They are used to provide enough support pressure against the borehole wall to keep it open for the service period which can vary depending on the borehole purpose. One of the main stability problems in formations with different strength layers is the considerable difference between the required mud pressures. Low leakage pressure requires a low drilling density to prevent lost circulation, while in hard rocks higher mud pressure is required to keep the borehole open [5]. Therefore, it is essential to determine the differences in failure pressure for poorly cemented granular formation and other stronger strata.

Laboratory tests are among the best suited methods for studying the borehole instability phenomenon. Number of researchers have utilised the thick-walled hollow cylinder (TWHC) specimens for studying the stability of underground openings such as tunnels, boreholes and oil wells. References [6] and [7] performed a series of TWHC tests on rocks to study the effect of anisotropic stress conditions on the behaviour of hard rocks. [8] investigated the macroscopic failure mechanism of synthetic rocks made of gypsum cement by conducting TWHC test. References [9], [10] carried out a valuable experimental study on the behaviour of Indiana limestone and consolidated Berea sandstone in the form of TWHC. References [11] and [12] conducted laboratory tests on the TWHC synthetic sandstone specimens and studied the effect of localised zones and different stress paths on borehole failure.

In this study, a number of TWHC laboratory tests were designed and performed on synthetic poorly cemented sand samples under controlled conditions. Status of the borehole wall was visually monitored by real-time camera recording in order to determine the point of first particle bonding breakage which leads to dislodging the particle from the borehole wall. The total potential and dissipative absorbed strain energy (modulus of toughness) was derived for different stress paths

S.S. Hashemi with the School of Engineering and Technology, Central Queensland University, Gladstone, Australia (phone: +61426111280; e-mail: s.hashemi@cqu.edu.au).

and cementation strengths and a failure criterion was introduced. This criterion is more precise than previously suggested criteria based on maximum strength of TWHC specimens, because the onset of borehole failure may take place either prior or after the peak strength of the specimen is reached. The results of this study give a more realistic insight into the actual failure behaviour of poorly cemented sandy formations, and they will help to design an enhanced support system to avoid borehole collapse both during drilling and after its completion.

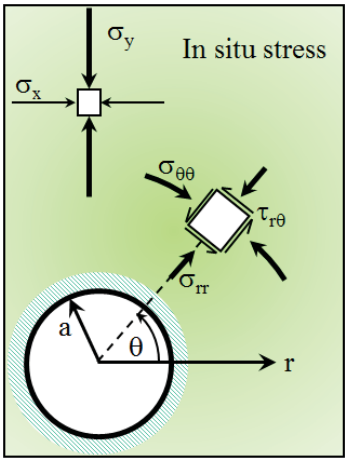

Fig. 1 Tangential (σ_θ) and radial (σ_r) stresses induced due to pre-existing far-field stresses around a drilled borehole

A. Induced Stresses around a Drilled Borehole

The in situ stress state can be defined in terms of the principal stresses, σ_v, σ_H, and σ_h. Fairhurst [13] showed that the maximum vertical stress can be calculated as the weight of the overlying layers at a certain depth and the minimum horizontal stress is estimated by in-field tests such as hydraulic fracturing and leak off tests [14]. Nevertheless, measuring the maximum horizontal stress (σ_H) is not straightforward and it can be estimated based on specific assumptions and considerations [15]-[17]. The tangential, radial and vertical stresses around a borehole may be calculated by different equations such as Kirsch equations based on principal stresses. In literature [18], [19], there are different closed form solutions for calculating stress and strain in a TWHC by the theory of elasticity. The principal stresses in a cylindrical coordinates system for a TWHC at any point of radial distance, r, are defined as,

$$\sigma_\theta = \frac{S_o D_o^2 - S_i D_i^2}{D_o^2 - D_i^2} + \frac{(S_o - S_i) D_i^2 D_o^2}{4r^2 (D_o^2 - D_i^2)} \quad (1a)$$

$$\sigma_r = \frac{S_o D_o^2 - S_i D_i^2}{D_o^2 - D_i^2} - \frac{(S_o - S_i) D_i^2 D_o^2}{4r^2 (D_o^2 - D_i^2)} \quad (1b)$$

$$\sigma_z = \frac{4F}{\pi (D_o^2 - D_i^2)} + \frac{S_i D_i^2}{(D_o^2 - D_i^2)} \quad (1c)$$

where σ_θ, σ_r and σ_z are the tangential, radial and vertical principal stresses respectively (Fig. 1), and S_i and S_o are the uniform internal and external stresses acting on the TWHC.

Stress-strain graphs were used to calculate the modulus of toughness. Although the "engineering" stress values can be easily obtained from the test results, in this study the "true" stresses were considered for deriving the precise strain energy values. In this approach, the actual diameter of the specimen in each step of the test was considered for calculating the stress.

II. Experimental Study

Investigation of subsurface sediments at a drilling site in South Australia showed that the layers above the bedrock are not homogeneous, i.e. the shallower layers of the sediment are composed of silt and fine sand, while the deeper layers of the sediments change to a dark grey plastic clay, and the problematic poorly cemented granular layer comes after this clayey layer. Based on the site investigation conducted by [20], the stress concentration around a borehole, low strength of the sandy layer and in some cases groundwater flow due to an aquifer near the drilling zone were identified as the major factors accounting for the borehole instability. Samples were collected from each metre of the unconsolidated sandy layer for further investigation. The pale yellowish-grey sand grains were mostly fine and sub-angular with random orientations. Thus, the specimens used for the laboratory tests were designed and prepared based on the sand grain size distribution and geometry obtained from the samples collected from this drilling site.

A series of physical model experiments for the TWHC samples was designed and conducted to investigate the failure mechanism of boreholes drilled through poorly cemented sandy formations. Also, unconfined compressive strength (UCS) and triaxial tests were performed on solid cylindrical specimens in order to obtain the mechanical properties of prepared specimens. The Hoek cell, pressure automatic maintainer and dependent gauges were modified in order to apply and measure low range stresses (i.e. maximum 5 MPa of confining pressure with 0.5 kPa accuracy) on specimens. To determine the point of particle bonding breakage at the borehole wall with respect to the stress-strain status of the specimen, the real-time borehole condition was visually monitored while applying the stresses on the specimen. Specimens were designed to fit into a HQ Hoek triaxial cell of 63.5 mm diameter and 127 mm length. The whole process of experimental studies and data analysis was effortful and time consuming, and took more than 18 months to complete.

A. Test Procedure and Plan

Three different stress paths were applied to the TWHC specimens to investigate the effect of stress paths on the borehole stability in poorly cemented sandy formations. Loading schedule was designed based on two approaches; (1) principal far-field stresses and (2) principal stresses at the borehole wall (See (2)). In the far-field based stress paths, the vertical stress (σ_z) and confining pressure (σ_{conf}) were considered and they both were increased simultaneously at the same rate up to certain level which simulated the hydrostatic condition acting on the specimens. Then, in the second step,

depending on the experiment plan the specimen was subjected either to a vertical loading increment (normal faulting) corresponding to a constant displacement rate of 0.07 mm/min or to a confining pressure increment (reverse faulting) corresponding to a constant pressure rate of 0.2 MPa/min. In the first path (2a) the magnitude of the confining pressure acting on the external surface of the specimens was kept constant during the second step of the test by an automatic pressure maintainer system.

$$1^{st}\text{ stress path } \begin{cases} \sigma_1 = \sigma_z > \sigma_2 = \sigma_3 = \sigma_{conf}\ (\text{far}-\text{field}) \\ \sigma_1 = \sigma_z > \sigma_2 = \sigma_\theta > \sigma_r = 0\ (\text{at borehole wall}) \end{cases} \quad (2a)$$

$$2^{nd}\text{ stress path } \begin{cases} \sigma_1 = \sigma_2 = \sigma_{conf} > \sigma_3 = \sigma_z\ (\text{far}-\text{field}) \\ \sigma_1 = \sigma_\theta > \sigma_2 = \sigma_z > \sigma_r = 0\ (\text{at borehole wall}) \end{cases} \quad (2b)$$

$$3^{rd}\text{ stress path } \begin{cases} \sigma_1 = \sigma_2 = \sigma_{conf} > \sigma_3 = \sigma_z\ (\text{far}-\text{field}) \\ \sigma_1 = \sigma_\theta > \sigma_2 = \sigma_z > \sigma_r = 0\ (\text{at borehole wall}) \end{cases} \quad (2c)$$

B. The Total Absorbed Strain Energy

In general, the elastic strain energy density can be calculated for a volume element subjected to arbitrary stress states as;

$$U_s^e = \frac{1}{2}\left(\sigma_{xx}\varepsilon_{xx} + \sigma_{yy}\varepsilon_{yy} + \sigma_{zz}\varepsilon_{zz}\right) + \left(\tau_{xy}\gamma_{xy} + \tau_{yz}\gamma_{yz} + \tau_{zx}\gamma_{zx}\right) \quad (3a)$$

Also, with respect to the principal axes for an elastic and isotropic body;

$$U_s^e = \frac{1}{2E}\left(\sigma_1^2 + \sigma_2^2 + \sigma_3^2 - 2\nu(\sigma_1\sigma_2 + \sigma_1\sigma_3 + \sigma_3\sigma_2)\right) \quad (3b)$$

On the other hand, we have;

$$U_s^e = U_{sv}^e + U_{sd}^e \quad (4a)$$

which;

$$U_{sv}^e = \frac{1-2\nu}{6E}(\sigma_1 + \sigma_2 + \sigma_3)^2 \quad (4b)$$

$$U_{sd}^e = \frac{1}{12G}\left[(\sigma_1 - \sigma_2)^2 + (\sigma_1 - \sigma_3)^2 + (\sigma_3 - \sigma_2)^2\right] \quad (4c)$$

where U_{sv}^e is the potential energy due to volume change and U_{sd}^e is the potential energy due to distortion. For instance, according to the von-Mises failure criterion the material failure occurs by the potential of the distortion strain energy density as;

$$U_s^e = U_d^e = \frac{4(1+\nu)}{6E}\tau_{oct}^2 \quad (5)$$

If the material failure is mainly controlled by the large plastic deformation process, the failure criterion should be defined as a plastic energy density failure criterion where the influence of porosities is negligible in a given failure volume. Thus,

$$U^p = \int_0^{\varepsilon^p} \sigma_{ij} d\varepsilon_{ij}^p = \int_0^{\varepsilon^p} q_{ij} d\varepsilon_{ij}^p + \int_0^{\varepsilon^p} \sigma_H d\varepsilon_{ii}^p = {U_c}^p \quad (6)$$

where $q_{ij} = \sigma_{ij} - \sigma_H \delta_{ij}$ and ${U_c}^p$ are the critical value of the plastic strain energy density which can be determined by laboratory tests [21], and for incompressible materials $\sigma_H d\varepsilon_{ii}^p \approx 0$. On the other hand, if the effect of the void coalescence cannot be ignored due to the generation of an unbalanced flow between the adjacent voids and considerable elastic strain energy, the damage dissipation failure criterion can be written as;

$$U^d = U^e\left(\frac{\bar{E}}{E} - 1\right) = U_c^d \quad (7)$$

where $\bar{E}$ is the undisturbed Young's modulus of the material, and U_c^d is the critical value of the damage dissipation density. [20] showed that the volumetric strain is not negligible ($d\varepsilon_{ii}^p \neq 0$) in poorly cemented sand specimens. When considering the principal stresses at the borehole wall in a 10 mm diameter borehole sample for different stress paths in the current test plan we have;

$$\sigma_1 = \sigma_z\ , \sigma_2 = \sigma_\theta = 2.05\ \sigma_{conf}, \sigma_3 = \sigma_r = 0 \quad (8)$$

Thus, (6) can be re-written as;

$$U^p = \int_0^{\varepsilon^p} \sigma_{ij} d\varepsilon_{ij}^p = \int_0^{\varepsilon^p} \sigma_z d\varepsilon_z^p + 2.05 \int_0^{\varepsilon^p} \sigma_{ii} d\varepsilon_l^p \quad (9)$$

where ε_z and ε_l are the vertical and lateral strains measured by strain gauges during the tests. As mentioned by [20], the poorly cemented sand specimens showed inelastic behaviour from the start of the second step in the conducted tests. Therefore, U^e in (2) has a minimal role when increasing the deviatoric stress.

After conducting further analysis of the camera recordings versus the obtained data, it was observed that the bonding breakage point did not occur at the peak stress. Since the debonding of sand particles at the borehole wall is a sign of the borehole failure initiation, these points were detected during the experiments. A failure criterion based on the total potential and dissipative strain energy densities (the modulus of toughness) was considered for each test on the TWHC based on the applied stresses. The total energy (i.e. potential and dissipative) was derived based on the results from the conducted tests. Fig. 2 shows the typical total potential and plastic dissipative strain energies for the first and second stress paths. According to Fig. 2 it can be written;

$$U^p + U^d + U_s^e = (A_1 + A_1') + (A_2 + A_2') \quad (10)$$

It should be mentioned that A_1' and A_2' were calculated based on an element at the borehole wall, because the principal stresses values at the borehole wall (σ_θ) are different from the far-field stresses (σ_{conf}). The modulus of toughness was calculated by the trapezoidal rule, which is a well-known numerical method. The trapezoidal rule works by approximating the region under the graph of a function as a trapezoid and calculating its area. Since during the test the data recording was performed for each 0.5 second, the area

under the stress-strain graph was calculated based on a high number of strips and the average error was 0.012% [22]. As shown in Fig. 2, the stress-strain relationship was almost linear until reaching the hydrostatic status (the first step of the experiments).

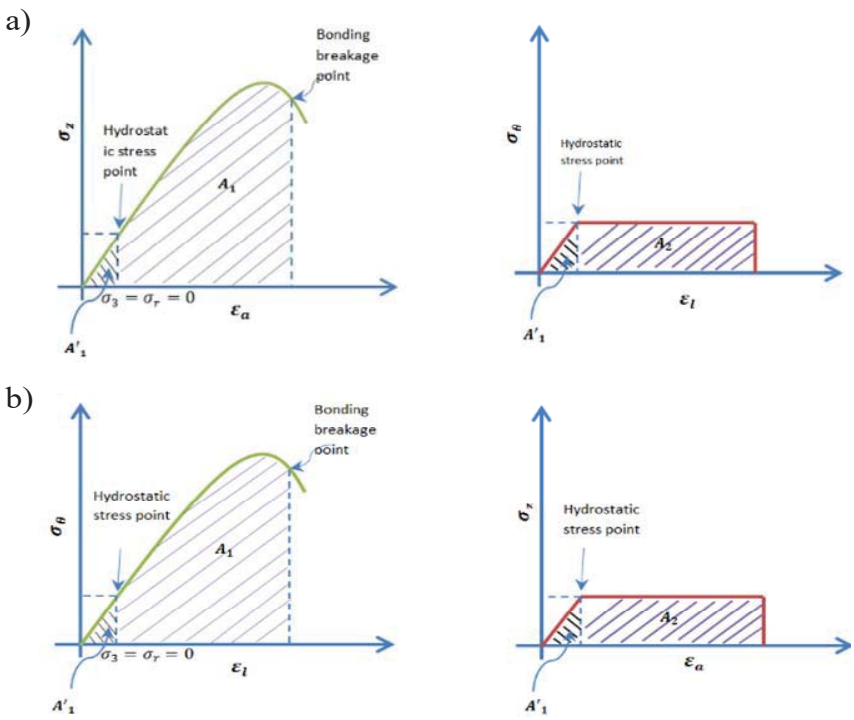

Fig. 2 Calculation process of the total strain energy from the stress-strain graphs for (a) first stress path, (b) second stress path

III. Results

A. Bonding Breakage Point Criterion Based on Strain Energy per Volume of Material

Bonding breakage between sand particles at the borehole wall occurs if the formation adjacent to the borehole is directly failed in tension or the aggregation of microcracks due to shear failure undergoes tension. [23] suggested that failure will occur when the distortional strain energy reaches a critical value which increases with the effective mean normal stress. In theory, the octahedral shear stress has a direct relationship with the strain energy. He proposed to consider the effective mean normal stress, $\sigma_{m,2}$, instead of σ_{oct} in the failure function, since the failure occurs in the direction of strike of the intermediate stress. The data from the laboratory tests were used to calculate $\sigma_{m,2}$ at the borehole wall in order to represent the trend of obtained data in the $U - \sigma_{m,2}$ domain.

As discussed in previous section, the bonding breakage points at the borehole wall were detected for various stress paths, cement values and borehole sizes. Then, based on the method which was elaborated in Section III, the total absorbed energy values per unit volume (ultimate toughness) were calculated for a single element at the borehole wall for each test. The principal stresses and the total absorbed strain energy were calculated based on the applied stresses at the boundary of the TWHC specimen. Since there was no supporting system deployed in the borehole, radial stress was considered to be zero in the current test program.

The total strain energy was derived based on the stress-strain diagram in the vertical and lateral directions. The effective mean normal stress, $\sigma_{m,2}$ at the borehole wall was calculated as;

$$\sigma_{m,2} = \frac{\sigma_1+\sigma_3}{2} \quad (11)$$

1. First Stress Path

The data from the experiments were used to calculate the principal stresses based on each stress path (2) applied to the specimens. The values of the total potential and dissipative energies per volume were plotted for the given value of w_c and different values of the intermediate principal stress as a function of $\sigma_{m,2}$. This mode of presentation was chosen to provide an insight into the behaviour of the total strain energy and with the thought that the criterion for the bonding breakage might have involved the value of the total strain energy to a linear function other than a power. Figs. 3 (a), (b) show the total strain energy versus the normal effective mean stress ($\sigma_{m,2}$) for each test conducted on 10 mm and 20 mm borehole size specimens for the first stress path, different cement contents (w_c= weight ratio of cement to sand grains) and confining pressures, respectively. According to Fig. 3, the relationship between the data in the $U - \sigma_{m,2}$ domain is relatively linear. Although it was possible to fit a polynomial equation to the obtained data with a good approximation, a linear relationship between the strain energy and $\sigma_{m,2}$ can be used for this material for different $\sigma_2 = \sigma_\theta$. All states of stress

below such a line are permissible states for which the borehole will not fail and those above it are not permissible because bonding breakage occurs before they can be attained. Any state of stress represented by a point on the line of constant w_c shows a limiting state of stress, from which the bonding strength, achieved by the value of $\sigma_{m,2}$ at that point. It is worth mentioning that the maximum confining pressure applied to the specimens (= 4 MPa) was based on the highest amount of stress that a TWHC specimen could withstand. In the case of applying $\sigma_{\text{conf}} > 5MPa$ the specimens with a maximum of $w_c = 8\%$ could not even meet the hydrostatic stress condition which was the first step of testing. As shown in Fig. 3, with an increase in the tangential stress the modulus of toughness increases for different cement contents. Also, increasing the w_c in the same path slightly shifts the failure envelope upward in most of the cases. However, the effect of the cement content is less considerable than the effect of the tangential stress in elevating the toughness. Fig. 3 (c) shows the toughness level versus the effective normal mean stress for 10 mm and 20 mm borehole size specimens for the first path. It shows that the relationship between the data in the $U - \sigma_{m,2}$ domain is almost linear for the 20 mm diameter borehole as well. [20], [24] showed that there is also a linear relationship between τ_{oct} and $\sigma_{m,2}$ in poorly cemented sands at maximum stress for the first stress path. As can be seen from Fig. 3 (c), the effects of the borehole size and cement content are considerable and comparison between the results suggests that the level of strain energy absorbed by the material until reaching the bonding breakage point is considerably lower in the 20 mm diameter borehole specimens, than in the 10 mm ones. For the test data plotted in the $U - \sigma_{m,2}$ domain, an arbitrary linear function can be defined as,

$$U = a + b\sigma_{m,2} \tag{12}$$

where a is the intersection of the line with the vertical axis (U) and b is the slope of the line. The constants in (12) were calculated from Fig. 3 (c) and are presented in Table I. It shows that, generally, the slope of trend lines for the 10 mm and 20 mm diameter borehole specimens are in a same range which suggests that the ratio of $\Delta U/\Delta\sigma_{m,2}$ is almost constant for both borehole sizes. As expected, due to size-scale effect suggested by [25], decreasing the size of the borehole diameter increases the failure stress in TWHC specimens.

TABLE I
CONSTANTS OF THE LINEAR EQUATION (12) FOR THE FIRTH STRESS PATH FOR THE TWHC SPECIMENS WITH 10 MM AND 20 MM DIAMETER BOREHOLES

Cement %	Borehole size (mm)	a	b	r^2
6	10	5.35	1.25	0995
7	10	2.68	1.72	0.961
8	10	3.35	1.75	0.935
6	20	-1.2616	1.15	0.993
7	20	-1.33	1.19	0.988
8	20	-3.15	1.52	0.981

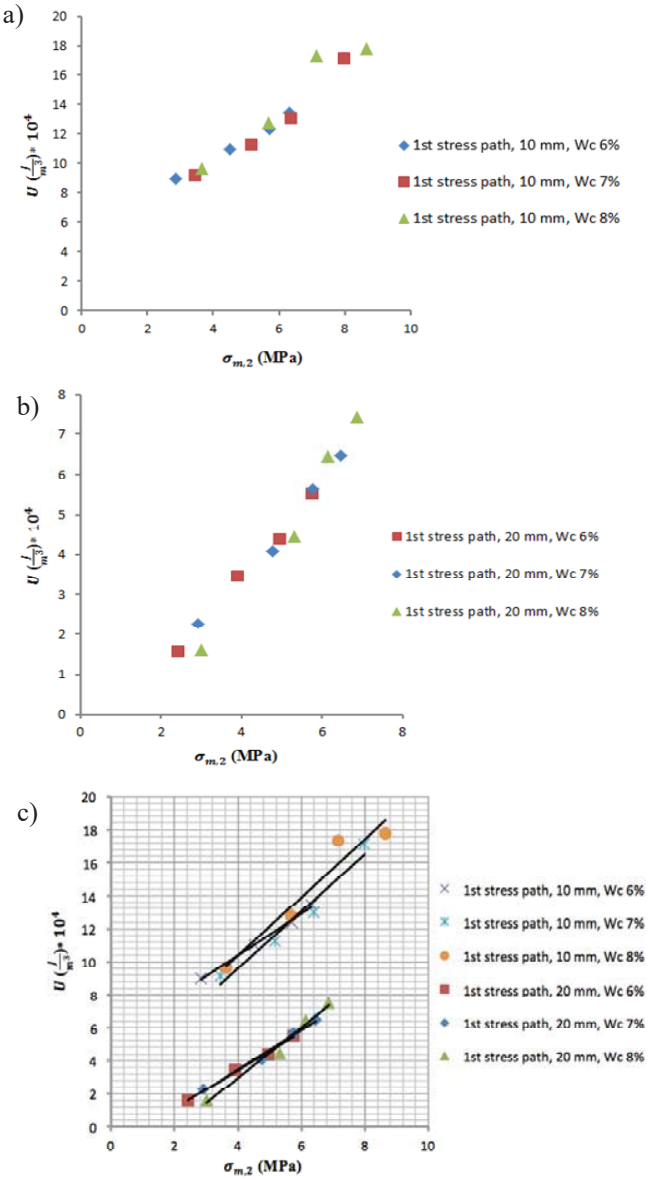

Fig. 3 Calculated total strain energy absorbed per volume of material (modulus of toughness) versus normal effective mean stress based on the results from laboratory tests conducted on TWHC specimens for the first stress path and different w_c in (a) 10 mm diameter borehole specimens, (b) 20 mm diameter borehole specimens, (c) 10 mm and 20 mm diameter borehole specimens

2. Second Stress Path

Fig. 4 represents the experimental data in the $U - \sigma_{m,2}$ domain for the second stress path where σ_θ was the maximum principal stress at the borehole wall. As mentioned in Section II *A*, the first and second stages of the experiments for the second path were based on the far-field stresses (σ_z and σ_{conf}) and the principal stresses were derived based on applied stresses on the boundary of the TWHC specimens. In the second stress path the majority of the energy absorbed in the lateral direction as expected and the vertical stress played minimal role in total energy. Likewise, linear equations with a good approximation could be fitted to the obtained data in the

$U - \sigma_{m,2}$ domain. As can be seen in Fig. 4, the toughness modulus level dramatically increases with increasing $\sigma_2 = \sigma_z$ in the second stress path for different w_c values.

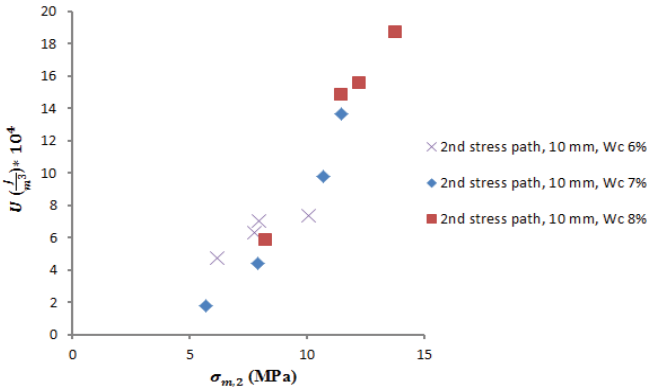

Fig. 4 Derived total strain energy absorbed per volume of material (modulus of toughness) versus normal effective mean stress based on the results from laboratory tests conducted on TWHC specimens for the second stress path and different w_c in 10 mm diameter borehole specimens

3. Third Stress Path

In the third stress path, σ_θ and σ_z were increased at the same rate until a certain value while keeping σ_z constant. In the second step σ_θ was increased until a bonding breakage point was observed at the borehole wall. The difference between the second and third stress paths is in the first stage of the experiment, which in the third path the magnitude of the confining pressure acting on the boundary of the specimen is considerably higher. Fig. 5 (a) shows the $U - \sigma_{m,2}$ for the third stress path. It is obvious from this graph that the relationship between the toughness modulus and the effective mean normal stress is almost linear again. Although with increasing w_c the strength of the specimen increases dramatically, the level of increment in the strain energy value was not reflected in that order and the effect of the cement content was not straightforward. Fig. 5 (b) demonstrates the effect of the borehole size for the third stress path. It shows that for the same w_c and σ_2, the amount of energy required for reaching the bonding breakage point in the 20 mm borehole size specimens is remarkably lower than for the 10 mm ones. Also, the slope of the trend line for both borehole sizes stayed almost unchanged which is consistent with the conducted experiments for the first stress path and a linear equation can be fitted for both borehole sizes.

In order to compare the results from the second and third stress paths, the test data in the $U - \sigma_{m,2}$ domain were superimposed for both stress paths as is shown in Fig. 6. As can been seen from Fig. 6, the data are located on a limited boundary and the slope of trend lines stays almost unchanged for both stress paths except for $w_c = 6\%$ in the second path which is considerably lower than the other results. For $\sigma_{conf} \geq 3$ MPa the specimens with the lowest strength (i.e. $w_c = 6\%$) underwent high σ_θ values in the initial stage of the tests for the second path. This may induce damage to the specimens and leaded to the lower toughness modulus in this cement content. Due to initially higher σ_θ values for the second stress path one would anticipate to observe a higher energy magnitude for it, however the graph shows that all data are scattered within the boundary and no dominancy was observed for the second and third paths in terms of the total absorbed energy. Since the borehole failure occurs mainly due to high σ_θ values, Fig. 6 shows that in the second and third stress paths the magnitude of σ_z at the initial stages of the tests does not affect the final toughness modulus in poorly cemented sand specimens. Fig. 6 also shows that an increase in w_c does not affect the strain energy level for these stress paths. This is an important outcome, since it shows that in this material the cement content will not affect the bonding breakage dramatically in unsupported boreholes when the σ_θ is the maximum principal stress.

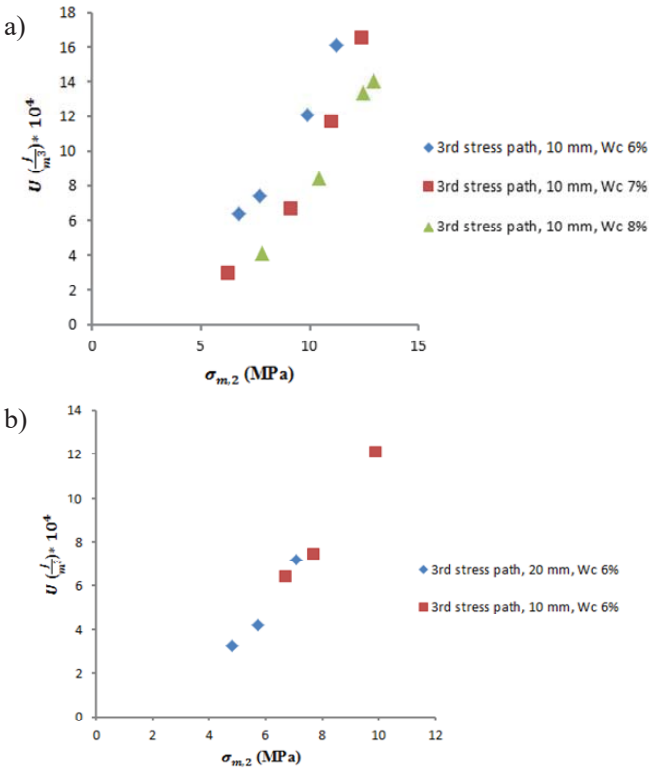

Fig. 5 Derived total strain energy absorbed per volume of material (modulus of toughness) versus normal effective mean stress based on the results from laboratory tests conducted on TWHC specimens for the third stress path and different w_c in (a) 10 mm diameter borehole specimens, (b) comparison between 10 mm and 20 mm diameter borehole specimens

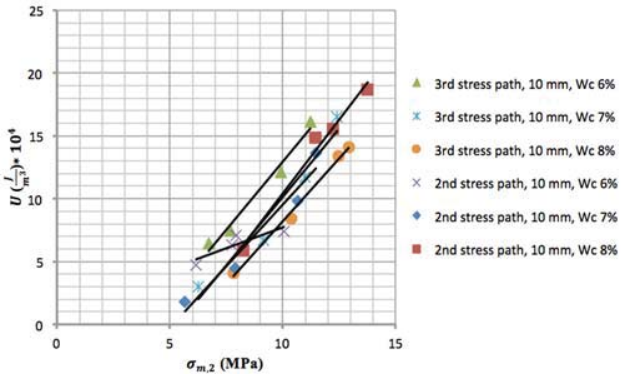

Fig. 6 Total strain energy absorbed per volume of material (modulus of toughness) versus normal effective mean stress based on the results from laboratory tests conducted on TWHC specimens for the second and third stress paths and different w_c in 10 mm diameter borehole specimens.

IV. Conclusion

The bonding breakage point at the borehole wall was detected by a micro camera which was deployed into the top platen of the Hoek cell to allow visual observation of the real-time status of the borehole during the test. The corresponding point on the stress-strain graph was identified. Then, the total strain energy per volume of material up to reaching the bonding breakage point was calculated for different applied stress paths in TWHC specimens. Two borehole diameter sizes (10 mm and 20 mm) and three different cement contents (6%, 7% and 8%) were considered versus three different stress paths.

Results showed that debonding points were located both before and after the peak maximum principal stress (σ_1) depending on the applied stresses and the cement contents. When the $\sigma_z = \sigma_1$ (first stress paths) for $\sigma_{conf} \leq 2\ MPa$ the debonding points were observed after the maximum principal stress (σ_1) for 10 mm and 20 mm borehole size specimens. In these cases there are two points with similar stresses and different strains on the $\sigma_1 - \varepsilon_1$ graph.

Modulus of toughness (U) for different stress paths was derived and plotted versus $\sigma_{m,2}$ as a borehole instability criterion. The relationship between the data in the $U - \sigma_{m,2}$ domain was relatively linear.

For the first stress path, with an increase in the tangential stress the total strain energy (toughness) increased for different values of w_c, while the effect of the cement content was less considerable than the effect of the tangential stress in increasing the toughness. Test results on 20 mm borehole size samples showed that the effect of the borehole size is considerable and the comparison between the results suggested that for the same w_c and σ_2, the level of strain energy absorbed by the material until reaching the bonding breakage point was much lower for the 20 mm diameter borehole specimens than for the 10 mm ones. However, the slope of trend lines in 10 mm and 20 mm borehole size specimens were similar. In the second stress path, where $\sigma_\theta = \sigma_1$, the majority of strain absorbed energy was in the lateral direction as expected. Likewise, linear equations could be fitted to the obtained data in $U - \sigma_{m,2}$ domain. Also, the toughness dramatically increased with elevating the $\sigma_2 = \sigma_z$ in the second stress path for different w_c values.

Despite of the remarkable influence of w_c on the strength of the specimens, the analyses showed that w_c will not dramatically affect the bonding breakage in the specimens when σ_θ was the maximum principal stress. The comparison between the second and third stress paths showed that the initial magnitude of σ_z, before achieving the hydrostatic status, did not affect the final toughness in poorly cemented sands while the final strengths for these paths varied.

Acknowledgments

This work has been supported by the Deep Exploration Technologies Cooperative Research Centre whose activities are funded by the Australian Government's Research Programme. This is DET CRC Document 2015/013.

References

[1] Lund, J.W., D.H. Freeston, and T.L. Boyd, Direct application of geothermal energy: 2005 worldwide review. Geothermics, 2005. 34(6): p. 691-727.
[2] Hashemi, S., A. Momeni, and N. Melkoumian, Investigation of borehole stability in poorly cemented granular formations by discrete element method. Journal of Petroleum Science and Engineering, 2014. 113: p. 23-35.
[3] Bratli, R.K. and R. Risnes, Stability and failure of sand arches. Society of Petroleum Engineers Journal, 1981. 21(02): p. 236-248.
[4] Hashemi, S., N. Melkoumian, and C. Xu. Effect of grain bonding on the stability of a borehole drilled through low cemented formations. in Proceedings: the 7th Australasian Congress on Applied Mechanics (ACAM 7), 9-12 December 2012, the University of Adelaide, North Terrace Campus/National Committee on Applied Mechanics of Engineers Australia. 2012. Engineers Australia.
[5] Tan, Q., J.G. Deng, and B.H. Yu, Study on Borehole Stability of Unconsolidated Sandstone in Depleted Reservior. Advanced Materials Research, 2013. 616: p. 720-725.
[6] Alsayed, M., Utilising the Hoek triaxial cell for multiaxial testing of hollow rock cylinders. International Journal of Rock Mechanics and Mining Sciences, 2002. 39(3): p. 355-366.
[7] Alsayed, M.I., Rock behaviour under multiaxial compression. 1996, Newcastle University.
[8] Perie, P. and R. Goodman. Evidence of new failure patterns in a thick-walled cylinder experiment. in Proc. 12th ETCE/ASME Conf. 1989.
[9] Ewy, R. and N. Cook. Deformation and fracture around cylindrical openings in rock—II. Initiation, growth and interaction of fractures. in International Journal of Rock Mechanics and Mining Sciences & Geomechanics Abstracts. 1990. Elsevier.
[10] Ewy, R. and N. Cook. Deformation and fracture around cylindrical openings in rock—I. Observations and analysis of deformations. in International Journal of Rock Mechanics and Mining Sciences & Geomechanics Abstracts. 1990. Elsevier.
[11] Hashemi, S. and N. Melkoumian, Effect of different stress path regimes on borehole instability in poorly cemented granular formations. Journal of Petroleum Science and Engineering, 2016. 146: p. 30-49.
[12] Hashemi, S., A. Taheri, and N. Melkoumian, An experimental study on the relationship between localised zones and borehole instability in poorly cemented sands. Journal of Petroleum Science and Engineering, 2015. 135: p. 101-117.
[13] Fairhurst, C., Stress estimation in rock: a brief history and review. International Journal of Rock Mechanics and Mining Sciences, 2003. 40(7): p. 957-973.
[14] Amadei, B. and O. Stephansson, Rock stress and its measurement. 1997: Springer.

[15] Zoback, M.D., et al., Well bore breakouts and in situ stress. Journal of Geophysical Research: Solid Earth (1978–2012), 1985. 90(B7): p. 5523-5530.
[16] Della Vecchia, G., et al., An analytical expression for the determination of in situ stress state from borehole data accounting for breakout size. International Journal of Rock Mechanics and Mining Sciences, 2014. 66(Complete): p. 64-68.
[17] Aadnoy, B.S., C. Gonsalves, and E. Kaarstad. Obtaining both horizontal stresses from wellbore collapse. in SPE/IADC Drilling Conference. 2013. Society of Petroleum Engineers.
[18] Obert, L. and W. Duvall, Rock mechanics and the design of structures in rock, 1967. 1967, Wiley, New York.
[19] Jaeger, J.C., N.G. Cook, and R. Zimmerman, Fundamentals of rock mechanics. 2009: John Wiley & Sons.
[20] Hashemi, S., A. Taheri, and N. Melkoumian, Shear failure analysis of a shallow depth unsupported borehole drilled through poorly cemented granular rock. Engineering Geology, 2014.
[21] Clift, S.E., et al., Fracture prediction in plastic deformation processes. International Journal of Mechanical Sciences, 1990. 32(1): p. 1-17.
[22] Atkinson, K., An introduction to numerical analysis. 1989. New York, 1991: p. 528.
[23] Mogi, K., Effect of the intermediate principal stress on rock failure. Journal of Geophysical Research, 1967. 72(20): p. 5117-5131.
[24] Al-Ajmi, A.M. and R.W. Zimmerman, Stability analysis of vertical boreholes using the Mogi–Coulomb failure criterion. International Journal of Rock Mechanics and Mining Sciences, 2006. 43(8): p. 1200-1211.
[25] Carpinteri, A., Size-scale effects in the failure mechanisms of materials and structures. 2002: CRC Press.